



Citation for published version:

Liu, L, Morton, YJ, Cheng, PH, Amores, A, Wright, CJ & Hoffmann, L 2023, 'Concentric Traveling Ionospheric Disturbances (CTIDs) Triggered by the 2022 Tonga Volcanic Eruption', *Journal of Geophysical Research: Space Physics*, vol. 128, no. 2, e2022JA030656. <https://doi.org/10.1029/2022JA030656>

DOI:

[10.1029/2022JA030656](https://doi.org/10.1029/2022JA030656)

Publication date:

2023

Document Version

Peer reviewed version

[Link to publication](#)

University of Bath

Alternative formats

If you require this document in an alternative format, please contact:
openaccess@bath.ac.uk

General rights

Copyright and moral rights for the publications made accessible in the public portal are retained by the authors and/or other copyright owners and it is a condition of accessing publications that users recognise and abide by the legal requirements associated with these rights.

Take down policy

If you believe that this document breaches copyright please contact us providing details, and we will remove access to the work immediately and investigate your claim.

23 **Abstract:** This paper investigates concentric traveling ionospheric disturbances (CTID) associated with
24 the Tonga volcanic eruption. Results show that: (1) Two types of CTID (CTID #1 and CTID #2) were
25 identified that traveled radially from Tonga at the speed of 610-880 m/s (acoustic-mode) and 300-380
26 m/s (Lamb-mode), respectively. CTID #1 reached 3800 km and 5000 km away from the eruption location
27 toward the directions of New Zealand and Australia, respectively. CTID #2 propagated persistently for
28 ~9 hours over New Zealand and Australia. (2) The CTID #2 wavefront changed after 08:35 UT over
29 New Zealand, possibly due to a combination of factors including the anisotropic propagation of CTID
30 #2, the regional geomagnetic declination, and westward-moving Lamb waves. (3) Topside TEC
31 enhancement with a magnitude over 2 TECu was observed from COSMIC-2 measurements. The
32 enhancement agrees with CTID #1 peak from nearby ground-based TEC observations and could be
33 related to the upward propagation of the F layer's CTID #1 signatures.

34
35 **Plain Language Summary:** The Tonga volcanic eruption on January 15 triggered various atmospheric
36 waves that propagate from the Earth's surface and throughout the atmosphere and ionosphere. In this
37 study, we discuss two types of concentric traveling ionospheric disturbances (CTID, #1 and #2)
38 propagating outward from the Tonga site based on measurements collected by ~1000 ground-based
39 global navigation satellite system (GNSS) receivers. Our analysis based on the CTID propagation speed
40 showed that CTID #1 and #2 traveled at acoustic and Lamb wave modes, respectively. We also analyzed
41 COSMIC-2 satellite radio occultation observations and showed that CTID #1-related enhancement
42 signatures were observed at the topside ionosphere near the eruption site. Moreover, it is interesting to
43 note that CTID #2 wavefront changed over New Zealand after 08:35 UT on January 15 likely followed
44 the regional geomagnetic declination and westward-moving Lamb waves.

46 1 Introduction

47 Volcanic eruptions can generate a broad spectrum of atmospheric pressure waves, including acoustic,
48 Lamb, and gravity waves. Acoustic waves propagate at the speed of ~330 m/s at the Earth's surface and
49 increase to 800–1100 m/s in the ionosphere (Afraimovich et al., 2002; Heki, 2006; Astafyeva, 2019; Aa
50 et al., 2022). Lamb waves are a type of non-dispersive atmosphere waves that propagate horizontally
51 above the Earth's surface with the speed of sound at ~300-350 m/s. However, they can cause ionospheric
52 perturbations through energy leakage from the troposphere to the ionosphere (Ogawa et al., 1982;
53 Mikumo et al., 1985; Kanamori et al., 1994; Heki, 2022; Zhang et al., 2022; Amores et al., 2022). Gravity
54 waves propagate upward obliquely at a much lower velocity (50-250 m/s) than the sound speed and reach
55 the ionosphere altitudes in ~45-60 minutes from the ground (Cheng and Huang, 1992; Artru et al., 2005;
56 Dautermann et al., 2009; De et al., 2011; Miller et al., 2015; Wright et al., 2022).

57 On January 15, 2022, a volcanic eruption occurred at Hunga Tonga-Hunga Ha'apai (20.5°S, 175.1°W,
58 hereafter simplified as Tonga) which triggered various atmospheric waves that propagate from the Earth's
59 surface throughout the atmosphere (Amores et al., 2022; Wright et al., 2022; Carvajal et al., 2022;
60 Otsuka, 2022). Several researchers have presented interesting findings associated with this event. For
61 example, Themens et al. (2022) identified two large-scale traveling ionospheric disturbances (TID) and
62 several subsequent mesoscale TIDs that propagated radially outward from the eruption site. Zhang et al.

63 (2022) found the Lamb-mode TID traveled around the Earth three times. Lin et al. (2022) showed that
64 concentric TIDs (CTID) were observed simultaneously over Australia and Japan because of the magnetic
65 conjugate effect. Heki (2022) reported that ionospheric disturbances passed over Japan at least four times
66 at the speed of Lamb waves, suggesting their origin as upward energy leakage from the troposphere. Aa
67 et al. (2022a) observed prolonged equatorial plasma bubbles over the Asia-Oceania area following the
68 arrival of Lamb waves. Astafyeva et al. (2022) estimated the Tonga eruption onset time and the released
69 energy based on ionospheric TEC observations. Saito (2022) observed two types of TIDs that arrived
70 over Japan about 3 and 7 hours after the eruption, respectively. Aa et al. (2022b) observed dramatic
71 suppression and deformation of the equatorial ionization anomaly (EIA) crests occurred in the American
72 sector after the Tonga volcano eruption. Ghent and Crowell (2022) detected supersonic acoustic, Lamb,
73 and tsunami signals over the southwestern Pacific using GNSS ionospheric observables.
74 In this study, we present additional observations of new features and analysis of the volcanic-induced
75 ionospheric effects. Using ground-based GNSS network measurements, we observed the presence of two
76 distinctive types of CTIDs. This is the first time the CTID wavefront change is observed over New
77 Zealand. Moreover, topside ionospheric TEC enhancement near the eruption site is reported for the first
78 time from low Earth orbit (LEO)-based COSMIC-2 observations.
79

80 2 Data and Methodology

81 Global navigation satellite system (GNSS) total electron content (TEC) observations used in this study
82 are calculated from ~1000 GNSS (GPS/GLONASS/BDS) receivers at a 30-second sampling rate. These
83 receivers are operated by the International GNSS Service (IGS) (Beutler et al., 1999), University
84 NAVSTAR Consortium (UNAVCO) (Ware et al., 2000), New Zealand GeoNet, and Australia GNSS
85 networks and are located in the region (50°S-10°N, 110°E-160°W). Figure S1 in the supporting
86 information (SI) file shows the locations of these receivers. An elevation mask of 15° from GNSS
87 receivers to satellites is used to mitigate potential multipath effects. The ionospheric piercing point (IPP)
88 height is set to be 300 km, which is around the height of the F2-layer peak electron density (hmF2)
89 according to radio occultation electron density profiles. Taking advantage of the quasi-invariant orbital
90 location of the BDS geostationary earth orbit (GEO) satellites C01, C03 and C04, ionospheric TEC
91 observations from BDS GEO receiver-satellite pairs are also used in this study to provide ionospheric
92 observations without being influenced by ionospheric spatiotemporal variations. To extract traveling
93 ionospheric disturbances (TID) signals from GNSS TEC observations, the detrended TEC (dT_{EC}) is
94 obtained by applying a Savitzky-Golay filter with a 40-minute sliding window (Savitzky and Golay,
95 1964; Zhang et al., 2017). The constellation observing system for meteorology, ionosphere, and climate
96 (COSMIC)-2 precise orbit determination (pod) TEC (podTEC) measurements, which are TEC values
97 above the LEO orbit altitude (550 km), were used to measure the response of the topside ionosphere. It
98 should be noted that only podTEC for elevation angles of the LEO-GPS link larger than 0° are used in
99 this study. In addition, infrared radiance (IR) imagery data from the 10.3 channel of the geostationary
100 operational environmental satellite (GOES)-17 were used to investigate the volcano-related Lamb wave
101 propagation in the lower atmosphere (30 km). GOES-17 is a geostationary satellite located above
102 (0°,137.2°W) at an orbit altitude of ~36000 km. It provides images of the Pacific region at spatial and

103 temporal resolutions of 2 km and 10 minutes, respectively (Schmit et al., 2017). To visualize the Lamb
104 wave structures from GOES-17 IR data, filter processing is applied in both temporal and spatial domains
105 to obtain the filtered IR observations (Amores et al., 2018 and 2022).

106

107 3 Results

108 3.1 Observations Using Ground-based GNSS Networks Near New Zealand and Australia

109 Figure 1 shows two-dimensional (2D) detrended TEC (dTEC) maps at nine selected time steps on
110 January 15, 2022. Full sets of 2D dTEC maps with a 15-minute interval are available in Movie S1 in the
111 SI file. Two distinctive CTIDs are characterized by different propagation speeds and will be analyzed in
112 detail in Figure 2. We denote the two CTIDs as CTID #1 and CTID #2, which are marked by black
113 arrows in Figure 1.

114 CTID #1 propagated radially outward from the Tonga eruption location and arrived over New Zealand
115 (2000-2500 km from the epicenter at 05:25 UT. The wavefronts of CTID #1 are aligned with the magenta
116 dashed line of great circles centered on the eruption. From 05:25 to 06:05 UT (see Movie S1 and Figures
117 1(a)-1(c)), CTID #1 propagated past New Zealand and its amplitude became attenuated at around 3500-
118 4000 km from the epicenter. Signatures matching that of CTID #1 reached the Australia sector (~140°E-
119 150°E) at 06:40 UT (Figure 1(e)). CTID #1 continued propagating outward at 06:55 UT (Figure 1(f))
120 and disappeared around 5000 km away from the epicenter over Australia. After 06:20 UT, CTID #2
121 started to appear in New Zealand and propagated radially outward over 4000 km away (see Figures 1(d)-
122 1(i) and Movie S1). After 07:45 UT (see Figures 1(g)-1(i) and Movie S1), clear CTID #2 signatures were
123 simultaneously observed over New Zealand and Australia and propagated outward persistently for
124 around 9 hours. It is interesting to note that the wavefront of CTID #2 in New Zealand is generally
125 aligned with the magenta dashed lines before 08:35 UT, but it comes into alignment with the black dashed
126 lines after 08:35 UT. The center of the black dashed curves (shown as a black cross) is located at (21.1°S,
127 178.6°E), which is west of the epicenter (20.5°S, 175.1°W). The IPP of the black cross is 660 km away
128 from the IPP of the magenta star. The change in CTID #2 wavefront will be further discussed in section
129 4.

130

131

132 Figure 2(a) shows the sound speed profile over a range of altitudes calculated from the Naval Research
133 Laboratory Mass Spectrometer and Incoherent Scatter Radar Exosphere (NRLMSISE-00) model (Picone
134 et al., 2002). According to the model, the theoretical propagation speed at 30 km (the lamb-mode in the
135 lower atmosphere) and 300 km (acoustic-mode in the ionosphere) is 321.7 m/s and 822.4 m/s,
136 respectively. Figures 2(c) and 2(d) show the dTEC plotted in UT vs. distance over New Zealand and
137 Australia, respectively. The distances are calculated from related IPP locations to the epicenter at 300
138 km altitude. IPP tracks used for generating Figures 2(c) and 2(d) are marked by blue curves and red
139 crosses in Figure 2(b), respectively.

140 We estimated the CTID propagation speed by tracing the slope of positive and negative wave structures
141 using linear regression in the UT-distance plots. Two groups of CTIDs (#1 and #2) were observed over
142 both the New Zealand and Australia regions (see oblique dashed yellow and green lines in Figures 2(c)
143 and 2(d)). In Figure 2(c), CTID #1 appeared around 05:25-06:30 UT at a speed of 700-860 m/s over New
144 Zealand and propagated as far as 3500-3800 km away from the epicenter around 06:30-06:50 UT at a
145 decreased speed of ~610 m/s. CTID #2 started to appear at 06:20 UT around 2300 km from the epicenter
146 and continued propagating outward over and beyond New Zealand at a speed of 300-380 m/s and lasting
147 for ~9 hours. In Figure 2(d), clear CTID #1 waves propagated 3800-5000 km, reaching Australia at a
148 speed of 700-880 m/s during 06:20-07:40 UT. CTID #1 over Australia was mixed with CTID #2 within
149 5000 km after 07:40 UT and became weakened and disappeared gradually by 08:00 UT. After 08:00 UT,
150 CTID #2 dominated with persistency at a speed of 340-360 m/s for more than 9 hours over Australia.
151 According to our speed estimation from the waves over New Zealand and Australia, CTID #1 propagated
152 at approximately 610-880 m/s, which matches the theoretical acoustic speed (822.4 m/s) in the
153 ionosphere from the NRLMSISE-00 model. It reached as far as 5000 km reaching Australia from the
154 volcanic eruption location. CTID #2 traveled with a speed of 300-380 m/s in the ionosphere and lasted
155 for around 9 hours over New Zealand and Australia. The propagation speed of CTID #2 is close to the
156 Lamb wave speed (321.7 m/s) in the lower atmosphere derived from the NRLMSISE-00 model. We note
157 that the dTEC magnitudes shown in Figures 1 and 2 are presented with saturated color scales to provide
158 a clear visualization of TID wavefronts. The real dTEC amplitudes are generally larger than those shown
159 in Figures 1 and 2 (see Figure S3 in the SI file for details).

160
161

162 **3.2 Observations using BDS GEO Satellite Measurements**

163 In addition to the CTID #1 signatures over New Zealand and Australia, slant TEC (sTEC) observations
164 from BDS GEO C01 and C04 satellites are used to verify CTID #1 signatures detected within 3000 km,
165 except for New Zealand. Figure 3(a) shows BDS GEO IPP locations at the azimuth of -135° to 90° within
166 3000 km from the eruption. Related GNSS receivers are marked by black dots. Figure 3(b) shows a
167 randomly selected sTEC time series during 04:00-10:00 UT from the line of sight between GNSS
168 receiver TUVA and BDS GEO satellite C01. This sTEC is in general decreasing. However, there are two
169 clearly identifiable local minima as marked by black and blue circles, respectively. The third point of
170 interest (red circle) is the beginning of the steep drop in sTEC, which led to the first local minimum. We
171 identified similar local minima and the beginning of the steep drop of sTEC for all sTEC profiles
172 computed from the BDS GEO C01 and C04 measurements. Figure 3(c) plots the IPP distances from the
173 epicenter against universal time (UT) for these three types of data points of interest. Propagation speeds
174 are estimated by fitting the slope using linear regression from these three types of data points. Results
175 show that the speeds estimated from dashed red, black, and blue lines (see Figure 3(c)) are all within
176 690-760 m/s, agreeing well with the CTID #1 speed derived from Figure 2. This means that the
177 ionosphere perturbations here (Figure 3) and for CTID #1 over New Zealand and Australia (Figure 2)
178 are the manifestation of the same TID in different azimuth directions. This also confirms the radial
179 propagation of CTID #1 from Tonga.

180
181

182 **3.3 COSMIC-2 Ionospheric Observations**

183 Figure 4(a) shows the paths of the LEO-based COSMIC-2 E2 satellite in the vicinity of the eruption site
184 over the Pacific Ocean on January 14 (cyan curve) and January 15 (blue curve). Topside TEC values
185 above the LEO satellite orbit (~530 km) derived from GPS G32 during 05:00-05:30 UT are plotted in
186 Figure 4(b). A topside TEC enhancement exceeding 2 TECu was detected in Figure 4(b) around 05:01-
187 05:15 UT on January 15. Similar topside ionospheric TEC enhancement structures were also observed
188 for other COSMIC-GPS links (see Figures S4-S6 of the SI file). No discernible topside ionospheric
189 enhancement can be identified on January 14. In Figure 4(d), the TEC from ground-based BDS GEO
190 C01 and C04 satellites increased sharply around 05:10-05:40 UT at nearby locations where the LEO-
191 based topside TEC enhancement structures were observed. Moreover, clear TEC enhancements can be
192 also observed from available GNSS stations distributed nearly 1000-1500 km from the volcanic eruption
193 location during 05:00-06:00 UT on January 15, 2022 (see Figures S7 and S8 of the SI file). This indicates
194 that TEC enhancements observed at the topside ionosphere and F layer height are correlated. It should
195 be noted that the enhancements observed from the ground-based TEC data are at roughly the same time
196 align the same great circle where the CTID #1 signals were detected, so the LEO-based topside TEC
197 enhancement is probably associated with CTID #1 of the F layer.

198
199

200 **3.4 Comparison with GOES-17 Observations**

201 Figure 5 compares the arrival time of the CTID #2 and the Lamb waves when they first reached New
202 Zealand and Australia. The arrival of CTID #2 observed from dTEC maps over New Zealand at 06:25
203 UT is shown in Figure 5(a), and the arrival time of the earliest Lamb wave captured by the GOES-17
204 filtered IR image in the same region is shown in Figure 5(b). There is a close agreement between CTID
205 #2 and Lamb waves in New Zealand in terms of arrival time, occurrence location, and spatial pattern
206 (see red arrows in panels (a) and (b)). Similarly, the CTID #2 observed over Australia at 07:45 UT is
207 well-aligned with the presence of the Lamb wave (see black arrows in panels (c) and (d)). These indicate
208 that CTID #2 is indeed associated with the propagation of the volcano-induced Lamb waves in the lower
209 atmosphere.

210
211

212 **4 Discussion and Conclusion**

213 Based on ground-based GNSS and LEO-based COSMIC-2 measurements, we identified two types of
214 CTID, CTID #1 and CTID #2, associated with the Tonga volcanic eruption on January 15, 2022. The

215 change of CTID wavefronts over New Zealand and the topside ionospheric TEC enhancement near the
216 eruption location are summarized below.

217 (1) According to the speed estimation over New Zealand (Figure 2(c)), Australia (Figure 2(d)), and the
218 Pacific Ocean (Figure 3), CTID #1 propagated radially at 610-880 m/s, which is close to the
219 theoretical acoustic velocity (822.4 m/s) at the ionospheric height calculated from the NRLMSISE-
220 00 model. Afraimovich et al. (2002), Heki (2006), and Astafyeva (2019) reported that the velocity
221 of shock acoustic waves in the ionosphere is 600-1100 m/s, which is consistent with the CID #1
222 speed estimated in this study. These suggest that the shock acoustic waves induced by the volcanic
223 explosion reached ionospheric altitudes and produced CTID #1, **though further study is still needed**
224 **to characterize the CTID #1 period which is expected to be less than the buoyancy period (Astafyeva,**
225 **2019).** Moreover, CTID #1 propagated outward from the volcanic eruption location as far as 3800
226 km and 5000 km away to reach New Zealand and Australia, respectively. To our best knowledge, it
227 is the first time that the acoustic-mode CTID associated with the volcanic eruption has been observed
228 to propagate such a long distance.

229 (2) The prevailing CTID #2 propagated persistently for around 9 hours over New Zealand and Australia
230 at a speed of 300-380 m/s (Figure 2), which is consistent with the speed estimated by Lin et al.
231 (2022), Zhang et al. (2022) and Themens et al. (2022) for this event. According to Amores et al.
232 (2022) and Otsuka (2022), the Lamb wave triggered by the Tonga volcanic explosion travelled
233 globally. Its propagation speed in the lower atmosphere, estimated by the NRLMSISE-00 model, is
234 321.7 m/s (Figure 2(a)), and from surface pressure and stratospheric nadir sounder observations is
235 310-320 m/s (Wright et al., 2022). The similarities in propagation speed suggest that the CTID #2
236 in the ionosphere is driven by the volcano-induced Lamb wave from the lower atmosphere.
237 Moreover, the Lamb wave captured by the GOES-17 IR data shows a similar spatial pattern and
238 arrival time with the CTID #2 over New Zealand and Australia. This also shows evidence that the
239 presence of CTID #2 is related to Lamb waves. CTID #2 could be caused by the upward energy
240 leakage into the ionosphere from Lamb waves either via resonance with the atmosphere during
241 propagation (Zhang et al., 2022; Heki, 2022; Ogawa et al., 1982) or by the stimulation of gravity
242 waves that are excited by the Lamb waves and ultimately travel at a propagation speed similar to
243 Lamb waves in the troposphere (Lin et al., 2022).

244 (3) The wavefronts of Lamb-mode CTID #2 over New Zealand before 08:35 UT are mostly aligned
245 with a great circle (magenta dashed line in Figure 1). After 08:35 UT, the wavefront is aligned with
246 a different great circle (black dashed line in Figure 1), which is located about 660 km west of the
247 epicenter. The change of the CTID #2 wavefront could be related to various factors:

248 • As the TID propagated outward for long distances, their wavefront may have shifted from the
249 original shape because of the anisotropic propagation characteristics of waves. **Moreover, the**
250 **polarization electric field (PEF) is generated in association with the TIDs (Huang et al., 1994;**
251 **Tsunoda, 2010; Zhang et al., 2019 and 2021).** **We believe that** the PEF embedded in the CTID #2
252 before 08:35 UT was able to help maintain the propagation direction of the original CTIDs. However,
253 the CTID #2 after 08:35 UT over New Zealand was characterized by smaller fluctuation amplitudes

254 than before (see Figure 3(b) in Zhang et al. (2022)), suggesting that the PEF was weakened to a level
255 that it could no longer maintain the TID original propagation direction. Subsequent TID propagation
256 over New Zealand would be guided by the distribution of the regional geomagnetic field lines where
257 the geomagnetic declination is around 22-26°. The geomagnetic declination is visually close to the
258 CTID #2 propagation direction after the wavefront change. Therefore, the regional geomagnetic
259 declination could be an important factor responsible for the CTID #2 wavefront change when the
260 PEF embedded in the CTID #2 gradually dissipated. Further study is still needed to investigate the
261 quantitative relationship between the CTID #2 wavefront change and geomagnetic declination.

262 • In addition to regional geomagnetic declination, the westward-moving Lamb waves could further
263 contribute to the wavefront change. The ionospheric disturbance center of CTID #2 coincides well
264 with the source center of the concentric Lamb waves from the GOES-17 filtered IR (see Figures 5(b)
265 and 5(d)) and AIRS brightness temperature perturbation measurements (see Figure S9 of the SI file).
266 Wright et al. (2022) also observed that the Lamb wave center was slightly to the west of the eruption
267 and moved further westward driven by prevailing easterly winds in the lower atmosphere. These
268 suggest that the westward-moving Lamb waves could also be responsible for the CTID #2 wavefront
269 change though its impacts could be secondary. Our investigation shows that the dusk terminator (see
270 Movies S2 and S3 in the SI file) and ionospheric shell heights (see Figure S10 in the SI file) have
271 negligible effects on the CTID #2 wavefront change observed in this study. **However, we caution**
272 **the reader that the wave activity at dusk has its day-to-day variability. Therefore, the analysis on**
273 **other days can only provide background references but not rigorous evidence of the negligible effects**
274 **of the dusk terminator on the wavefront change.**

275 (4) The TEC enhancement structures were simultaneously observed by ground-based BDS GEO TEC
276 (Figures 3(b) and 4(d), and Figures S7-S8 of the SI file) and LEO-based COSMIC-2 podTEC (Figure
277 4(b) and Figures S4-S6) measurements. This means that this enhancement is the same structure that
278 appeared at both the F-layer ionosphere (300 km) and the topside ionosphere (above 530 km). From
279 Figure 3, we know that the clear TEC enhancement before 06:00 UT is a manifestation of the CTID
280 #1 peak in the F layer, so the LEO-based TEC enhancement is likely to be the signature of the CTID
281 #1 in the topside ionosphere (above 530 km) through the upward propagation of CTID #1.

282 Acknowledgments

283 This project is sponsored by NASA grant 80NSSC21K1156. CJ Wright is supported by a Royal Society
284 University Research Fellowship (UF160545 and URF\R\221023) and NERC grant NE/S00985X/1. The
285 authors are grateful for the constructive comments provided by the anonymous reviewers and for the
286 useful discussion with Dr. Ercha Aa and Dr. Weijia Zhan in revising the manuscript.

287 The GNSS data used in this study are available from University NAVSTAR Consortium (UNAVCO)
288 (<https://data.unavco.org/archive/gnss/>), Crustal Dynamics Data Information System (CDDIS)
289 (<https://cddis.nasa.gov/>), New Zealand GeoNet (<https://data.geonet.org.nz/gnss/>), Australia GNSS
290 networks (<https://gnss.ga.gov.au/network>), respectively. The constellation observing system for

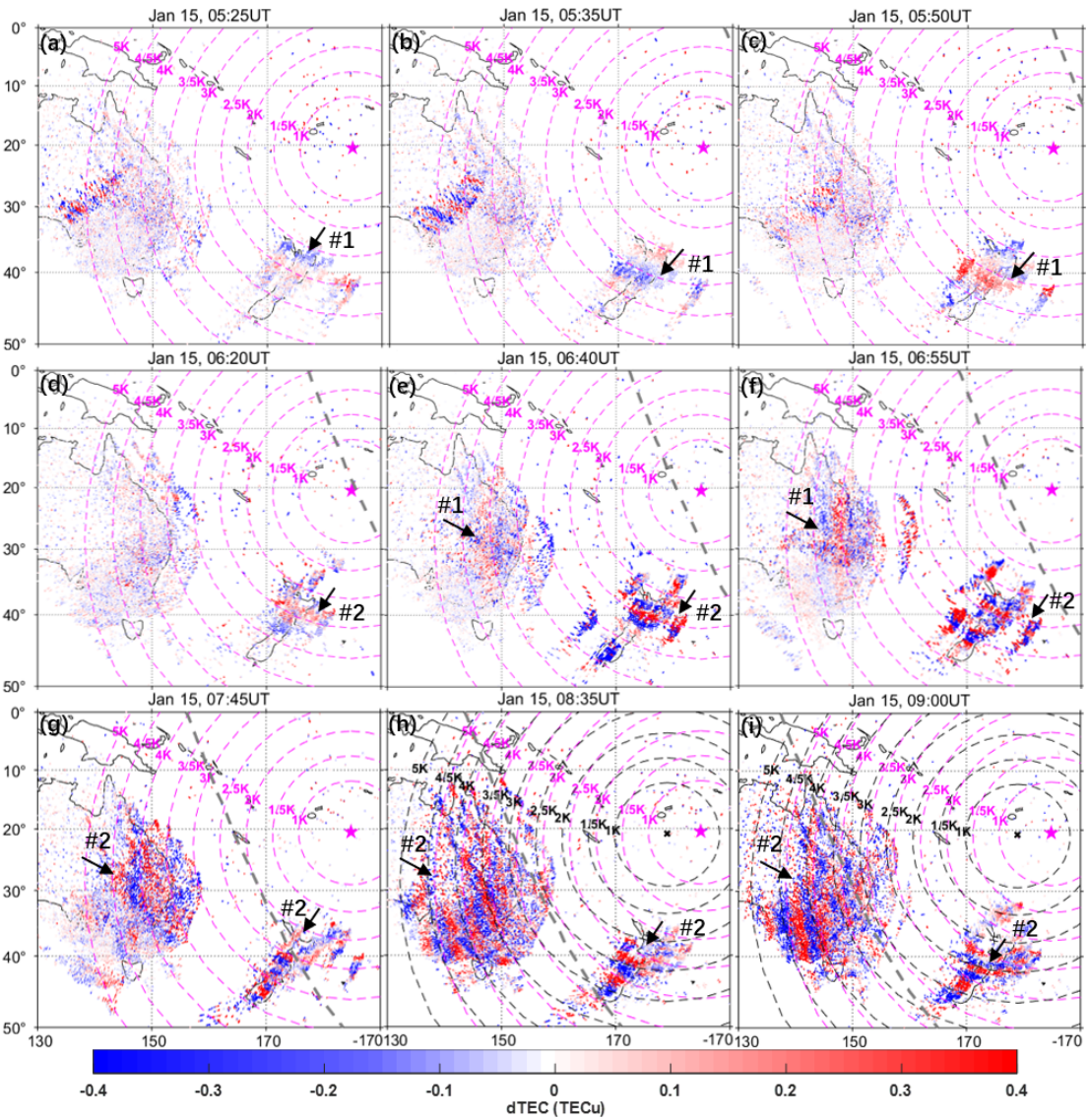
291 meteorology, ionosphere, and climate (COSMIC)-2 podTEC measurements are available from
292 <https://data.cosmic.ucar.edu/gnss-ro/cosmic2/>. The Geostationary Operational Environmental Satellite
293 (GOES)-17 infrared radiance data are from [https://home.chpc.utah.edu/~u0553130/Brian_Blalock/cgi-](https://home.chpc.utah.edu/~u0553130/Brian_Blalock/cgi-bin/goes16_download.cgi)
294 [bin/goes16_download.cgi](https://home.chpc.utah.edu/~u0553130/Brian_Blalock/cgi-bin/goes16_download.cgi). The Advanced Infrared Sounder (AIRS) aboard NASA's Aqua satellite
295 brightness temperature perturbation data are from [https://datapub.fz-](https://datapub.fz-juelich.de/slcs/airs/gravity_waves/data/projects/tonga/)
296 [juelich.de/slcs/airs/gravity_waves/data/projects/tonga/](https://datapub.fz-juelich.de/slcs/airs/gravity_waves/data/projects/tonga/).
297

298 Reference

- 299 [1] Aa, E., Zhang, S.-R., Erickson, P. J., Vierinen, J., Coster, A. J., Goncharenko, L. P., et al. (2022a).
300 Significant ionospheric hole and equatorial plasma bubbles after the 2022 Tonga volcano eruption.
301 *Space Weather*, 20, e2022SW003101. <https://doi.org/10.1029/2022SW003101>
- 302 [2] Aa, E., Zhang, S.-R., Wang, W., Erickson, P. J., Qian, L., Eastes, R., et al. (2022b). Pronounced
303 suppression and X-pattern merging of equatorial ionization anomalies after the 2022 Tonga volcano
304 eruption. *Journal of Geophysical Research: Space Physics*, 127, e2022JA030527.
305 <https://doi.org/10.1029/2022JA030527>
- 306 [3] Afraimovich, E. L. (2008), First GPS-TEC evidence for the wave structure excited by the solar
307 terminator, *Earth Planets Space*, 60, 895–900.
- 308 [4] Afraimovich, E. L., Kosogorov, E. A., & Plotnikov, A. V. (2002). Shock–acoustic waves generated
309 during rocket launches and earthquakes. *Cosmic Research*, 40(3), 241–254.
310 <https://doi.org/10.1023/A:1015925020387>
- 311 [5] Amores, A., Jordà, G., Arsouze, T., & Le Sommer, J. (2018). Up to what extent can we characterize
312 ocean eddies using present-day gridded altimetric products? *Journal of Geophysical Research:*
313 *Oceans*, 123(10), 7220–7236.
- 314 [6] Amores, A., Monserrat, S., Marcos, M., Argüeso, D., Villalonga, J., Jordà, G., & Gomis, D. (2022).
315 Numerical simulation of atmospheric Lamb waves generated by the 2022 Hunga - Tonga volcanic
316 eruption. *Geophysical Research Letters*, e2022GL098240.
- 317 [7] Artru, J., Ducic, V., Kanamori, H., Lognonné, P., & Murakami, M. (2005). Ionospheric detection
318 of gravity waves induced by tsunamis. *Geophysical Journal International*, 160(3), 840–848.
- 319 [8] Astafyeva, E. (2019). Ionospheric detection of natural hazards. *Reviews of Geophysics*, 57(4),
320 1265–1288.
- 321 [9] Astafyeva, E., Maletckii, B., et al. (2022) The 15 January 2022 Hunga Tonga eruption history as
322 inferred from ionospheric observations, *ESSOAr*, doi: 10.1002/essoar.10511226.1,
323 <https://doi.org/10.1002/essoar.10511226.1>
- 324 [10] Beer, T. (1978). On atmospheric wave generation by the terminator. *Planetary and Space*
325 *Science*, 26(2), 185–188.
- 326 [11] Carvajal, M., Sepúlveda, I., Gubler, A., & Garreaud, R. (2022). Worldwide signature of the 2022
327 Tonga volcanic tsunami. *Geophysical Research Letters*, e2022GL098153.
- 328 [12] Cheng K, Huang YN (1992) Ionospheric disturbances observed during the period of Mount
329 Pinatubo eruptions in June 1991. *J Geophys Res* 97(A11):16995. doi:10.1029/92JA01462

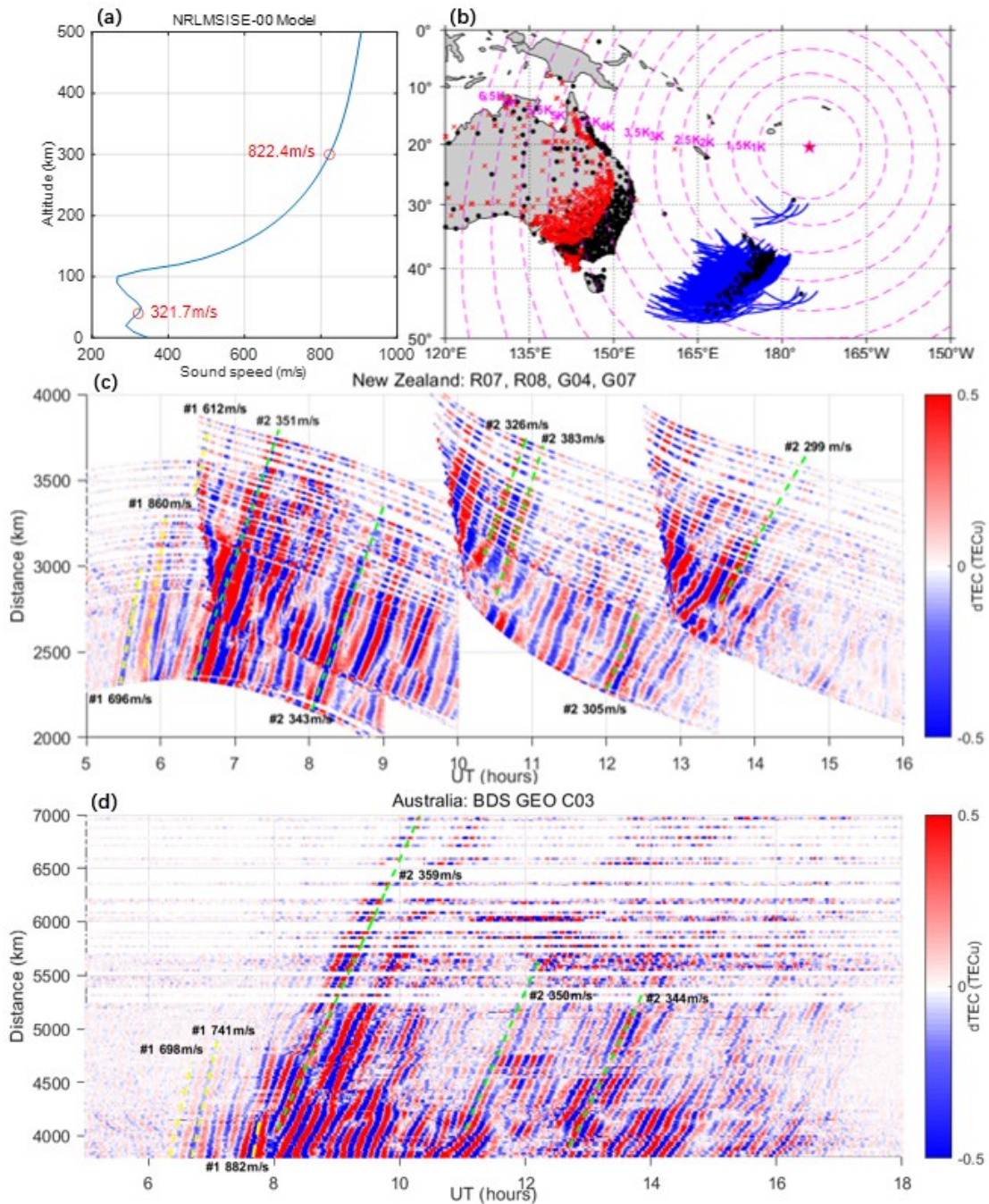
- 330 [13] Dautermann, T., Calais, E., Lognonné, P., & Mattioli, G. S. (2009). Lithosphere-atmosphere-
331 ionosphere coupling after the 2003 explosive eruption of the Soufriere Hills Volcano, Monserrat.
332 *Geophysical Journal International*, 179(3), 1537–1546. <https://doi.org/10.1111/j.1365-246X.2009.04390.x>
333
- 334 [14] De Angelis, S., McNutt, S. R., & Webley, P. W. (2011). Evidence of atmospheric gravity waves
335 during the 2008 eruption of Okmok volcano from seismic and remote sensing
336 observations. *Geophysical Research Letters*, 38(10).
- 337 [15] Forbes, J. M., S. L. Bruinsma, Y. Miyoshi, and H. Fujiwara (2008), A solar terminator wave in
338 thermosphere neutral densities measured by the CHAMP satellite, *Geophys. Res. Lett.*,35, L14802,
339 doi:10.1029/2008GL034075
- 340 [16] Ghent, J. N., & Crowell, B. W. (2022). Spectral characteristics of ionospheric disturbances over the
341 southwestern Pacific from the 15 January 2022 Tonga eruption and tsunami. *Geophysical Research*
342 *Letters*, 49, e2022GL100145. <https://doi.org/10.1029/2022GL100145>
- 343 [17] Heki, K. (2006). Explosion energy of the 2004 eruption of the Asama Volcano, central Japan,
344 inferred from ionospheric disturbances. *Geophysical Research Letters*, 33(14).
- 345 [18] Heki, K. (2022). Ionospheric signatures of repeated passages of atmospheric waves by the 2022
346 Jan. 15 Hunga Tonga eruption detected by QZSS-TEC observations in Japan. DOI:
347 <https://doi.org/10.21203/rs.3.rs-1448599/v1>
- 348 [19] Huang, C.-S., C. A. Miller, and M. C. Kelley (1994), *Basic properties and gravity wave initiation*
349 *of the midlatitude F region instability*, *Radio Sci.*, 29, 395–405, doi:10.1029/93RS01669.
- 350 [20] Kanamori H, Mori J, Harkrider DG (1994) Excitation of atmospheric oscillations by volcanic
351 eruptions. *J Geophys Res* 99:21947–21961
- 352 [21] Lin, J.-T., Rajesh, P. K., Lin, C. C. H., Chou, M.-Y., Liu, J.-Y., Yue, J., . . . Kung, M.-M. (2022).
353 Rapid Conjugate Appearance of the Giant Ionospheric Lamb Wave in the Northern Hemisphere
354 After Hunga-Tonga Volcano Eruptions. *Earth and Space Science Open Archive*, 18. Retrieved from
355 <https://doi.org/10.1002/essoar.10510440.2> doi: 10.1002/essoar.10510440.2
- 356 [22] Mikumo, T. and Bolt, B. A. (1985). Excitation mechanism of atmospheric pressure waves from the
357 1980 Mount St Helens eruption. *Geophysical Journal International* 81, 445–461
- 358 [23] Miller, S. D., Straka, W. C., Yue, J., Smith, S. M., Alexander, M. J., Hoffmann, L., et al. (2015).
359 Upper atmospheric gravity wave details revealed in nightglow satellite imagery. *Proceedings of the*
360 *National Academy of Sciences of the United States of America*, 112(49), E6728–E6735.
361 <https://doi.org/10.1073/pnas.1508084112>
- 362 [24] Ogawa, T., Kumagai, H., & Sinno, K. (1982). Ionospheric disturbances over Japan due to the 18
363 May 1980 eruption of Mount St. Helens. *Journal of Atmospheric and Terrestrial Physics*, 44(10),
364 863-868.
- 365 [25] Otsuka, S. Visualizing Lamb waves from a volcanic eruption using meteorological satellite
366 Himawari-8. *Geophysical Research Letters*, e2022GL098324.
- 367 [26] Picone, J. M., A. E. Hedin, D. P. Drob, and A. C. Aikin (2002), NRLMSISE-00 empirical model of
368 the atmosphere: Statistical comparisons and scientific issues, *J. Geophys. Res.*, 107(A12), 1468,
369 doi:10.1029/2002JA009430.

- 370 [27] Saito, S. (2022). Ionospheric disturbances observed over Japan following the eruption of Hunga
371 Tonga-Hunga Ha'apai on 15 January 2022. *Earth, Planets and Space*, 74(1), 1-9.
- 372 [28] Savitzky, A. and Golay, M. J. E. (1964). Smoothing and differentiation of data by simplified least
373 squares procedures. *Analytical Chemistry* 36, 1627–1639
- 374 [29] Schmit, T. J., Griffith, P., Gunshor, M. M., Daniels, J. M., Goodman, S. J., & Lebar, W. J. (2017).
375 A closer look at the ABI on the GOES-R series. *Bulletin of the American Meteorological*
376 *Society*, 98(4), 681-698.
- 377 [30] Themens, D. R., Watson, C., Žagar, N., Vasylyevych, S., Elvidge, S., McCaffrey, A., ... &
378 Jayachandran, P. T. (2022). Global propagation of ionospheric disturbances associated with the
379 2022 Tonga Volcanic Eruption. *Geophysical Research Letters*, e2022GL098158.
- 380 [31] Tsunoda, R. T. (2010). On seeding equatorial spread F: Circular gravity waves. *Geophysical*
381 *Research Letters*, 37(10). <https://doi.org/10.1029/2010GL043422>
- 382 [32] Wright, C., Hindley, N., Alexander, M. J., Barlow, M., Hoffmann, L., Mitchell, C., et al. (2022).
383 Surface-to-space atmospheric waves from Hunga Tonga-Hunga Ha'apai eruption. *Earth and Space*
384 *Science Open Archive*. <https://www.essoar.org/doi/10.1002/essoar.10510674.2>
- 385 [33] Zhang S-R, Vierinen J, Aa E, Goncharenko LP, Erickson PJ, Rideout W, Coster AJ and Spicher A
386 (2022) 2022 Tonga Volcanic Eruption Induced Global Propagation of Ionospheric
387 Disturbances via Lamb Waves. *Front. Astron. Space Sci.* 9:871275. doi:
388 10.3389/fspas.2022.871275
- 389 [34] Zhang, S. R., Coster, A. J., Erickson, P. J., Goncharenko, L. P., Rideout, W., & Vierinen, J. (2019).
390 Traveling ionospheric disturbances and ionospheric perturbations associated with solar flares in
391 September 2017. *Journal of Geophysical Research: Space Physics*, 124(7), 5894-5917.
- 392 [35] Zhang, S. R., Erickson, P. J., Gasque, L. C., Aa, E., Rideout, W., Vierinen, J., ... & Coster, A. J.
393 (2021). Electrified postsunrise ionospheric perturbations at Millstone Hill. *Geophysical Research*
394 *Letters*, 48(18), e2021GL095151.
- 395 [36] Zhang, S. R., Erickson, P. J., Goncharenko, L. P., Coster, A. J., Rideout, W., & Vierinen, J. (2017).
396 Ionospheric bow waves and perturbations induced by the 21 August 2017 solar eclipse. *Geophysical*
397 *Research Letters*, 44(24), 12-067.
- 398
399
400



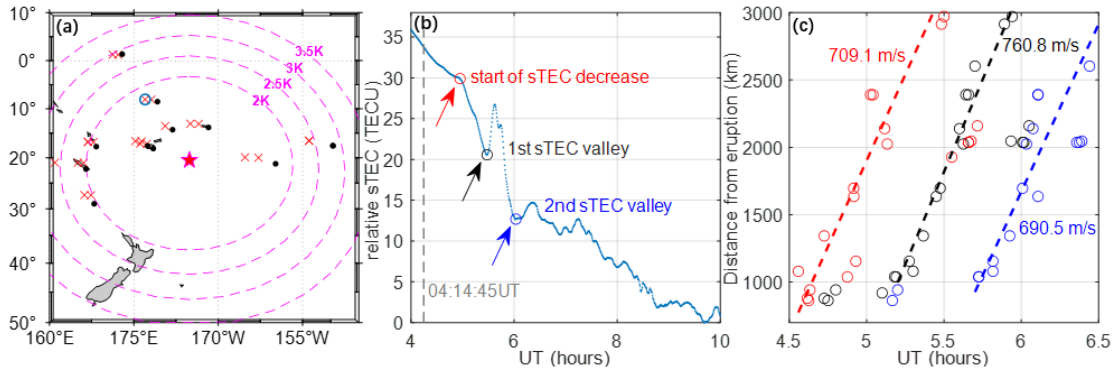
401
 402
 403
 404
 405
 406
 407
 408
 409
 410
 411

Figure 1. 2D maps of dTEC at nine selected time steps from 05:25 UT to 9:00 UT on January 15, 2022. The magenta star represents the Tongva volcanic eruption epicenter (20.5°S, 175.1°W). The black cross in panels (h) and (i) corresponds to the location of the “ionosphere disturbance center” (21.1°S, 178.6°E), which is fitted based on the wavefront of dTEC maps after 08:35 UT (see details in Figure S2 and Table S1 in the SI file). The iso-distance circles separated at 500 (0.5K) km intervals marked by dashed magenta and black lines are the great circles at an altitude of 300 km from the location of the volcanic eruption and ionospheric disturbance center, respectively. The gray dashed line indicates the location of the solar terminator. Full sets of 15-minute 2D dTEC maps on January 15 are available in Movie S1 of the SI file.



412
 413
 414
 415
 416
 417
 418
 419
 420
 421
 422

Figure 2. (a) The sound speed profile at various altitudes calculated from the NRLMSISE-00 model. The propagation speed at altitudes of 30 km and 300 km is marked by red circles. (b) IPP tracks over New Zealand and Australia. The blue curves and red crosses are the IPP locations derived from GNSS (GLONASS R07, R08, and GPS G04, G07) and BDS GEO (C03) satellites, respectively. The black dots are the locations of GNSS receivers. (c) The plot of the dTEC UT-distance from the volcanic eruption location for GLONASS (R07, R08) and GPS (G04, G07) satellites over New Zealand. (d) Similar to panel (c) but derived from BDS GEO C03 satellite over Australia. The CTID propagation velocity is marked by the oblique dashed black line in panels (c) and (d).



423

424

Figure 3. (a) BDS GEO satellite IPP distributions (red crosses) at the azimuth of -135° to 90° within

425

3000 km from the volcanic eruption location. These IPPs are calculated from BDS GEO satellites (C01

426

and C04) and available ground-based GNSS receivers in the area (shown as black dots). The cyan circle

427

represents the IPP derived from the line of sight between GNSS receiver TUV A and BDS GEO C01. (b)

428

An example of relative sTEC time series (cyan curves) between TUV A and C01. The time of sTEC

429

starting to decrease, the first and second sTEC valleys are marked by red, black, and blue circles,

430

respectively. The vertical dashed gray line represents the onset time of the Tonga volcanic eruption. (c)

431

Arrival time of sTEC perturbations as a function of the distance from the volcanic eruption location. Red,

432

black, and blue circles represent the arrival times of three types of ionosphere perturbations of the panel

433

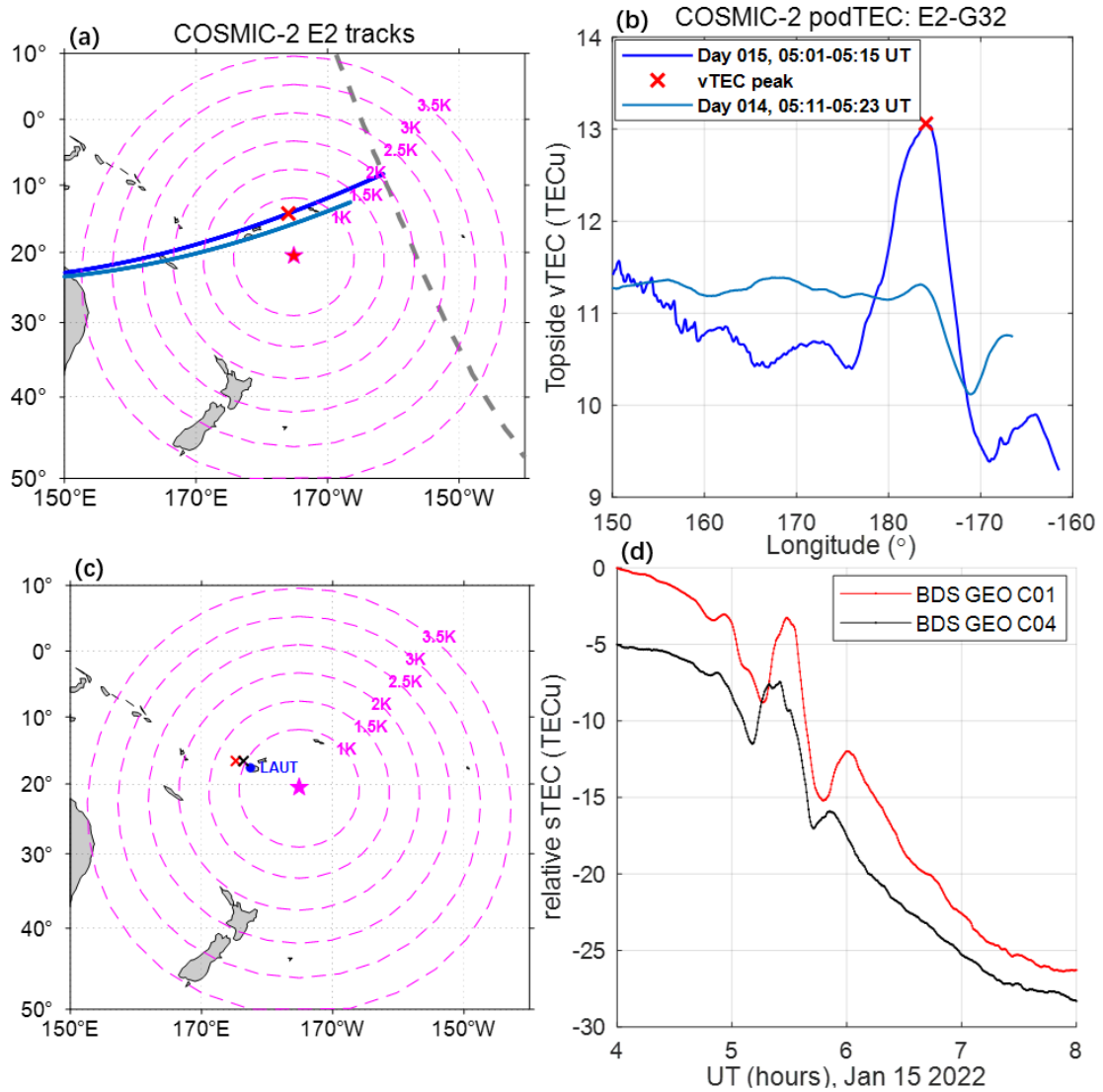
(b). Linear regression is performed to estimate the TID propagation speed, which is marked by oblique

434

red/black/blue dashed lines.

435

436



437

438 **Figure 4.** (a) COSMIC-2 E2 satellite tracks during 05:00-05:30 UT on January 15 (blue curves) and

439 January 14 (cyan curves). The gray dashed line represents the solar terminator around 05:10 UT. (b)

440 Topside podTEC variations during 05:00-05:30 UT for these two days. The TEC peak on January 15 is

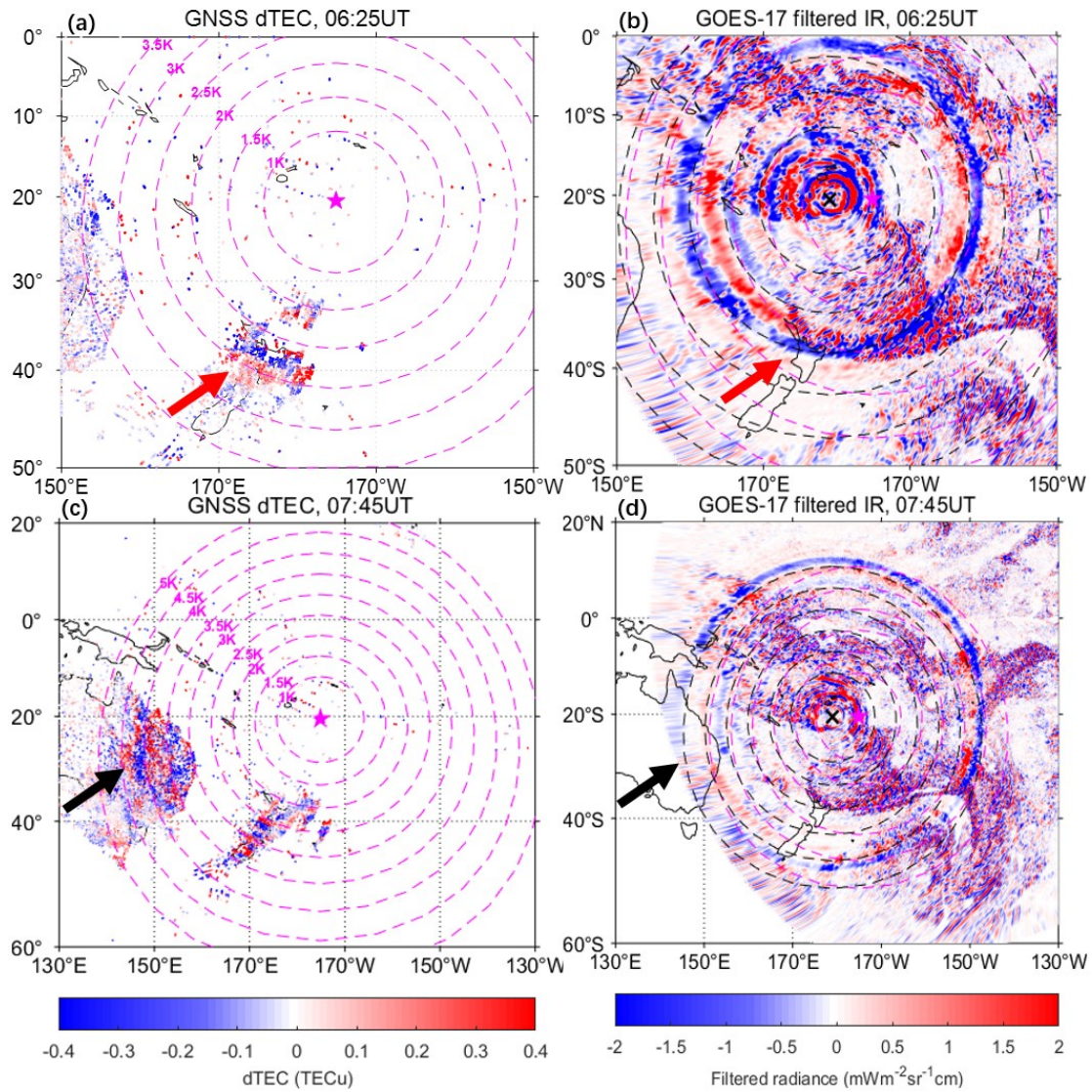
441 marked by the red cross in panels (a) and (b). (c) BDS GEO C01 (red cross) and C04 (black cross) IPP

442 locations for LAUT station (blue dot). (d) Relative TEC temporal variations of BDS GEO C01 (red curve)

443 and C04 (black curve) satellites during 04:00-08 UT on January 15, 2022.

444

445



446

447

448

449

450

451

452

453

454

455

456

457

Figure 5. (a) CTID wavefronts at 300 km (ionospheric height) observed from GNSS dTEC maps at 06:25 UT on January 15, 2022. (b) Concentric Lamb waves at 30 km (stratospheric height) visualized by the GOES-17 filtered IR imagery at 06:25 UT on January 15, 2022. (c) and (d) Similar to (a) and (b), but at 7:45 UT. The dominant CTID and Lamb waves are marked by red arrows in (a) and (b) when arriving over New Zealand (06:25 UT), while they are marked by black arrows in (c) and (d) when arriving over Australia (7:45 UT). The volcanic eruption location and ionospheric disturbance center are marked by the magenta star and black crosses, respectively. Great circles altitude for GNSS dTEC (magenta dashed lines in panels (a) and (c)) and GOES-17 IR maps (magenta/black dash lines in panels (b) and (d)) are set to be 300 km and 30 km above the Earth, respectively.